

Article

# Analysing the Influence of Fibers on Fresh Concrete Rheometry by the Use of Numerical Simulation

Florian Gerland , Tim Vaupel , Thomas Schomberg and Olaf Wünsch

Department of Fluid Dynamics, University of Kassel, 34125 Kassel, Germany

\* Correspondence: florian.gerland@uni-kassel.de (F.G.); t.vaupel@uni-kassel.de (T.V.)

**Abstract:** Measuring the flow properties of fiber-laden fresh concrete poses a substantial challenge because not only the fraction of fibers but also their orientation process during the measurement influence the measured quantities. Numerical simulations of the flow in a ball probe rheometer are used to determine the fiber orientation process during the measurement of the flow properties and its influence on the measured variables. Through analytical considerations and comparison with measurement results, it can be shown that the constitutive law applied can reproduce the real flow behavior very well, taking the fiber orientation into account. At the same time, it is investigated why no orientation influence on the torque is recognizable in the experimental measurement curves, although the orientation process demonstrably exceeds the duration of the measurement process. The results show that fluid inertia is overcome before the recognizable onset of fiber orientation, and the spatially inhomogeneous flow minimises the impact of the orientation process on torque. The simulation model aligns well with experimental outcomes, indicating a linear increase in effective viscosity with increasing fiber volume fraction. The findings can be used to accurately measure the objective material parameters of the orientation-considering constitutive law using ball probe rheometers, so that an accurate prediction of the flow process of fresh concrete with fibers is made possible, for example for the simulation of formwork fillings.

**Keywords:** fiber orientation; fresh concrete rheology; orientation prediction; anisotropy; orientation tensors



**Citation:** Gerland, F.; Vaupel, T.; Schomberg, T.; Wünsch, O. Analysing the Influence of Fibers on Fresh Concrete Rheometry by the Use of Numerical Simulation. *Constr. Mater.* **2024**, *4*, 128–153. <https://doi.org/10.3390/constrmater4010008>

Received: 20 November 2023

Revised: 17 January 2024

Accepted: 19 January 2024

Published: 25 January 2024



**Copyright:** © 2024 by the authors. Licensee MDPI, Basel, Switzerland. This article is an open access article distributed under the terms and conditions of the Creative Commons Attribution (CC BY) license (<https://creativecommons.org/licenses/by/4.0/>).

## 1. Introduction

This article deals with the modeling and numerical simulation of the flow behavior of fresh concrete. The mathematical description and the numerical simulation of the flow behavior of fibre reinforced fresh concrete require a sufficiently accurate qualitative and quantitative measurement of the flow behavior. However, the dependence of the flow properties on the fiber orientation represents a central challenge for the measurement and constitutive description of the flow behavior of fiber suspensions such as fresh concrete, because the adjustment of the fiber orientation in measuring apparatuses beyond the position in the shear plane is rarely feasible and the measurement of the orientation is also rarely possible and usually complex. In the field of fresh concrete rheometry, there are various measuring devices to overcome the problem. The ball probe rheometer is widely used. A representative device of this type is visualized in Figure 1. To measure the flow properties, a ball in a cylindrical sample container is moved on a circular path around the cylinder axis and the applied speed-dependent torque is measured. Related types of this device use a cylinder or other simple geometries as the measuring body. Although all established rheometer manufacturers have devices of this type in their product range, they are not standardized in terms of geometric dimensions. In addition, there is no analytical description of the flow field. As a result, objective material parameters cannot be calculated directly from the raw data (torque vs. rotational speed), even for fiber-free fresh concretes.

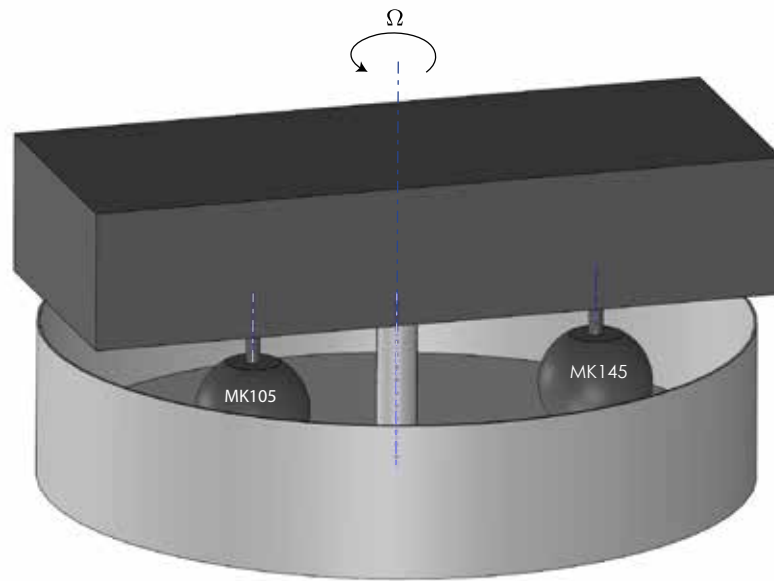


**Figure 1.** Examined ball probe rheometer eBT2 from Schleibinger Testing Systems Teubert u. Greim GmbH. with two ball probes.

On the basis of a dimensional analysis and a numerical parameter study, we were nevertheless able to determine the general relationship between the measured variables torque  $M$  and rotational speed  $\Omega$  with the objective Bingham material parameters yield stress  $\tau_y$  and plastic viscosity  $\mu$  with the coefficients of the approximation function  $(a_0, a_1, a_2)$  in a previous paper despite the lack of an analytical solution [1].

By reinserting the dimensioned variables into the correlation function, the following relationship is obtained, where  $l$  is the diameter of the circular path of the ball probe and  $D$  is the diameter of the sample container. For further details, see [1]

$$M = l^2 \mu \Omega D \left( a_0 + a_1 \left[ \frac{\tau_y l}{\mu \Omega D} \right]^{a_2} \right) \quad (1)$$

The numerical investigation of a fiber suspension in a Couette flow showed that the fiber orientation process is much slower than overcoming the inertia of the matrix fluid [2]. As a result, a steady-state of a fiber suspension flow is reached much later than for the same type of matrix liquid without fibers. The slow orientation process in the Couette flow also had a direct effect on the development of the torque. In contrast, the experimental investigations of fiber suspensions in ball probe rheometers in [3] did not show any such orientation effects in the  $M$ - $\Omega$  measurement curves, although at least qualitatively during the measurements a comparably slow orientation process was observed as in the numerical investigations of the Couette flow.

In addition to the flow geometry, the experimental investigation on ball probe rheometers and the numerical investigation of the Couette flow show another significant difference. The investigations of the Couette flow were carried out at a constant rotational speed, so that the change in torque over time can be attributed exclusively to the orientation and the associated change in the stress state. In the experiments in the ball probe rheometers, however, the rotational speed followed time-linear ramp functions. The stress state is therefore already time-dependent without the fiber effect due to the time dependence of the rotational velocity.

On the one hand, it is therefore checked whether the constitutive law presented in Section 2.1 in conjunction with the orientation model presented in Section 1.2 can represent the measured torque-rotational speed relations. On the other hand, it will be investigated why no clear orientation-dependent effects in the torque can be identified in

the measurements. In order to answer this question, the temporal development of the flow at constant rotational speed is also investigated in the ball probe rheometer.

### 1.1. Experimental Investigations of Fiber Suspensions

*Ouari et al.* investigated the flow behavior of fiber-reinforced fresh mortar [4]. They used a Vane cell for this purpose. The slenderness ratio is introduced here to compare different fiber sizes in the published sources. The following applies:  $a_r = L/2R$  with the fiber length  $L$  and the fiber diameter  $2R$ . To avoid misunderstandings, the diameter of the fiber is given as  $2R$  and the diameter of the sample container as  $D$  which is shown in Equation (1). The polypropylene fibers had a slenderness ratio  $a_r = 111$  with an average fiber length of 3.33 mm and the suspension could be measured in the rheometer up to a maximum fiber content of 1 m.-%. The gap between the Vane element and the sample cup was approximately three fiber lengths. To interpret the torque-rotational speed relation, the authors used a calibration method that does not take local exceeding of the yield point into account. They found only a small effect of the fibers on the plastic viscosity. Only from a fiber content of 5 m.-% a significant increase in the yield point was observed. The authors described the observed yield point increase as linear, although the data range shown could also be explained by a non-linear, e.g., exponential dependence. From a mass fraction of the fibers of 1 m.-%, homogeneous sample mixing was hardly possible. At a mass fraction of the fibers of 0.5 m.-%, the authors initially observed a slight reduction in the yield point and interpreted that the fibers partially destroy the cement hydration products and agglomerations. They therefore explained the reduction in the yield point at low fiber content by a change in the matrix fluid.

In a recent paper by Wang et al., steel fibers in concrete were investigated experimentally [5]. On the one hand, different fiber types were compared with the result that milled steel fibers resulted in a higher flexural and tensile strength of the hardened concrete compared to hook-shaped and wave-shaped fibers. Secondly, and most importantly for the classification of this work, the tensile and flexural strength of the milled steel fibers was investigated as a function of the volume fraction at constant aspect ratio of 60 to 80. In the range of 0.6 vol.-% and 1.5 vol.-%, the greatest bending and tensile strength of the hardened concrete was found. If fibers are added to the concrete above this limit, the mechanical properties decrease. The reason given by the authors is the tendency to agglomeration, which reduces the compactness of the concrete. This paper deals with the entire area in which fluid mechanical measurements and numerical simulations are useful. However, it should be noted again that for the application of steel fibers in concrete a range in small quantities is useful.

For further classification of this paper, a look should be taken at the paper by Villar et al. [6]. In this work, experiments were carried out to evaluate parameters that contribute to the induced torque. Different fresh cement mortar mixes, different aspect ratios and different fiber geometries were investigated. It was found, among other things, that steel fibers deform more strongly elastically at an aspect ratio of over 45. This deformation facilitates the alignment of the fibers. In this work, fibers with an aspect ratio of 30 were used in the experiments as well as in the numerical investigations. (See Section 2.1) Accordingly, the elastic deformation was not investigated in this paper and was neglected in the numerical calculations.

In a paper on the development of a yield point model for fiber-reinforced granular systems such as fresh concrete, Martinie et al. investigated cement mortar in a concrete rheometer and found an increase in shear stresses during the start-up process [7]. The fibers were randomly distributed in the unshaped sample. Even in the steady state, the authors observed a significantly increased shear stress (at the same shear rate) compared to the fiber-free cement mortar. They explained the increase in stress by a fiber orientation in the direction of flow that occurs over time. The significant increase in stress in the steady state is caused by contact networks between the grains of the granular medium and the fibers. The packing density in the granular medium is decisive for the occurrence and magnitude

of a yield point in the fiber-free state. The higher the packing density, the greater the friction between the granular components and therefore the higher the yield point of the mixture. If additional fibers are added, an even stronger network is created, which binds both the fibers and the granular components of the matrix fluid. This results in a significant increase in the yield point of the fiber suspension, especially if the packing density of the granular medium is already close to the maximum packing density.

### 1.2. Numerical Investigations of Fiber Suspensions

Based on some of the experimental research work presented, models for fiber suspensions were formulated both with and without taking orientation into account. Another important branch of research, however, does not use experimental results as a basis for modeling, but analytical considerations, which are transferred to models of the fiber suspension. The cell method is particularly noteworthy. The central assumption of the method is that the flow is undisturbed outside a near field around the cylindrical fiber. Based on the relative velocity of fluid and fiber in the far field (i.e., outside the flow disturbed by the fiber in the cell), the fiber wall shear stress is then described, assuming the no-slip condition at the fiber. From this wall shear stress at the individual fibre, it is possible to generalize from the individual fibre to a fibre distribution using suitable relationships (so-called Kramer expression). The method is described in detail in [8].

Using the described procedure, Férec et al. was able to prove that the Folgar-Tucker equation for Newtonian fluids (without fiber diffusion model) can also be constructed without formulating the moment of the orientation probability density function of the Jeffery equation (cf. [9]). In the same way, the authors then derived corresponding orientation models using the flow functions of different shear-thinning fluids (e.g., Power-Law, Ellis, Carreau) [8]. For this class it could be shown that the Jeffery orientation equation or the Folgar-Tucker equation is also valid, but the fiber stress components differ from the Newtonian fluid. Analytical investigations of a planar shear flow showed a changed orientation behavior of the fibers in the shear-thinning matrix fluid compared to the Newtonian fluid. In contrast to the Newtonian matrix, an orientation component in the third direction also remains in the steady state orientation. In addition, the fiber stress fraction decreases with increasing shear thinning of the matrix fluid.

Férec et al. investigated basic flow patterns in a Newtonian matrix fluid using the Fokker-Planck equation [10]. The authors investigated various axisymmetric flow forms such as pipe flow, the swelling exit from a nozzle as in plastic 3D printing (swelling) or the squeezing flow between parallel circular disks (center-gated disk flow). The authors compared the solution of the complete, three-dimensional Fokker-Planck equation with the solution of the Folgar-Tucker equation in conjunction with the IBOF-5 closure approximation and were able to show that only negligibly small deviations occur between the two solution methods for all investigated flow forms. In addition, the influence of momentum coupling between fluid and fibers was investigated in the form of the fiber constitutive law. It was observed that the difference in the orientation with and without consideration of the fiber tension term is small, while significant differences in the velocity fields were identified. In the pipe flow, the stronger orientation of the fibers on the wall compared to the axis of rotation causes a flattening of the velocity profile similar to a shear-decelerating fluid. Based on these findings, we also use the numerically efficient formulation using the IBOF-5 closure for the following investigations.

### 1.3. Current Research Question

Fiber orientation plays an important role in current research. One exciting topic is fiber orientation in 3D printing processes of fiber-reinforced concrete. To this end, the work of Reinold et al. numerically investigates how the fibers in concrete orient themselves in a 3D printing process [11]. Since there is a strong shear during this process, the fibers are increasingly aligned in the direction of printing. This effect is advantageous for achieving targeted fiber alignment in the finished component. Explicit attention is paid to the influ-

ence of the process parameters in order to achieve the most predictable fiber orientation possible in the finished component. It was found that a higher printing speed and a smaller nozzle diameter lead to an increased fiber orientation in the printing direction, as there is then a higher shear in the printing process.

Other tests commonly used in the field of materials science, such as the cone test, were investigated numerically by Thanh et al. [12]. What is special about this investigation is that the fibers are simulated as connected mortar particles, i.e., as highly flexible fibers. This work offers an exciting and simple method that can predict the fiber orientation of flexible fibers well.

The work of Zhao et al. offers another very challenging field of investigation, which looks more at the real pouring processes and their fiber orientation [13]. In this work, the pouring process of fiber-reinforced self-compacted concrete into a formwork was investigated. A CFD model was set up to investigate the formwork pouring process and to see what influence the pouring point and the dimensions of the formwork have on the orientation of the fibers in the process and in the finished component. A further work that deals with the casting process of fiber-reinforced components is the work of Rienesl et al. [14]. Various metamodels are set up, the parameters of which are calibrated using experimentally molded injection-molded parts that have previously been examined using computed tomography at regions of interest. This dependency is intended to illustrate how complex this topic is, as it is directly dependent on the components that are to be produced with it.

This is where this work comes in and offers a new method to investigate fiber orientation numerically and experimentally. The numerical investigation, which shows very similar results to the experiments, shows that the numerical simulation can reproduce the real fiber orientation in this complex flow field very well and thus has great potential to be used in other complex flows as well.

The numerical work presented here forms the basis for the numerical modeling used here. The findings listed in the experimental work are to be subjected to a deeper physical explanation on the basis of the results presented in the following.

## 2. Materials and Methods

### 2.1. Governing Equations and Constitutive Modeling of Fiber Reinforced Concrete

A class of constitutive laws for fiber suspensions up to the medium concentration regime is known from the field of short fiber reinforced plastic composites [15]. Most laws allow a separation of the effect of matrix fluid and fibers of the form

$$\mathbf{S} = -p\mathbf{I} + \mathbf{T}^m + \mathbf{T}^f, \tag{2}$$

with pressure  $p$  and the identity tensor  $\mathbf{I}$ , where  $\mathbf{T}^m$  represents the extra stresses caused by the matrix fluid and  $\mathbf{T}^f$  the extra stresses caused by the fibers.

For modeling the flow function of particle suspensions in general and fresh concrete in particular, the Bingham material model

$$\dot{\gamma} = \begin{cases} 0 & \text{if } |\tau| \leq \tau_y \\ \frac{|\tau| - \tau_y}{\mu} \operatorname{sgn} \tau & \text{if } |\tau| > \tau_y. \end{cases} \tag{3}$$

is widely used [15]. Below the yield stress  $\tau_y$ , the Bingham material behaves like a solid, i.e., it is not sheared at all. If the yield stress is exceeded, the Bingham material begins to flow. The shear stress then increases linearly with the shear rate  $\dot{\gamma}$ . The definition of the flow function

$$\eta(\dot{\gamma}) := \frac{\tau}{\dot{\gamma}} \tag{4}$$

as a quotient of shear stress and shear rate allows the generalization of Newton’s material law  $\tau = \eta\dot{\gamma}$  for shear rate-dependent constitutive laws. For the Bingham constitutive law it reads

$$\eta_{Bm}(\dot{\gamma}) = \frac{\tau_y}{\dot{\gamma}} + \mu. \tag{5}$$

Note that the complete constitutive law for Bingham matrix fluids such as fresh concrete is presented, whereby the special case of the Newtonian matrix fluid is directly included in the case of negligible yield stress in Equation (5).

Analogous to Newton’s constitutive law, the generalization with the flow function is also formulated three-dimensionally isotropically, so that the main directions of stresses and distortion velocities match. The generalized three-dimensional constitutive law is then as follows

$$\mathbf{T}^m = 2\eta(\dot{\gamma})\mathbf{D} \tag{6}$$

with the generalized shear rate  $\dot{\gamma}$ ,

$$\dot{\gamma} := \sqrt{2\mathbf{D} : \mathbf{D}}. \tag{7}$$

where  $\mathbf{D}$  is the strain rate tensor.

Equation (5) shows a singularity of viscosity for vanishing shear rates ( $\lim_{\dot{\gamma} \rightarrow 0} \eta_{Bm}(\dot{\gamma}) = \infty$ ). The singularity requires special treatment in the numerical realization of the constitutive law.

The constitutive model developed by Férec et al. for fiber suspensions with Bingham matrix fluids [16] is based on the slender body theory and the cell model. The validity of the model is limited to low and medium concentration regime. Furthermore, a constant velocity gradient along the fiber surface (i.e., on the scale of the fiber length) and quasi-steady fluid motion (i.e., creeping flow) are assumed. To derive the extra stresses induced by the fibers, the velocity profile within the cell is calculated from the momentum balance and using the Bingham material model. From this, the wall shear stress and the viscous force acting on the individual fiber can be determined by integration over the fiber surface. Using the Kramer expression, volume averaging of this force leads to the fiber extra stress fraction  $\mathbf{T}^f$ , taking into account the fiber concentration and the orientation of the individual fibers. The formulation of the stresses caused by the fibers depends on the local Bingham number. If the fluid within the cell is completely sheared ( $Bm \ll 1$ ), the following applies

$$\mathbf{T}^f = \mu\phi \frac{2a_r^2}{3 \ln(h/R)} \mathbf{D} : \mathbf{A}_4 + \tau_y\phi \frac{a_r(h/R - 1)}{\ln(h/R)} \mathbf{A}_2. \tag{8}$$

Here  $h$  is the cell radius,  $R$  the fiber radius,  $\mu$  the plastic viscosity and  $\tau_y$  the yield stress of the matrix liquid. The symmetric tensors  $\mathbf{A}_2$  (rank 2) and  $\mathbf{A}_4$  (rank 4) are statistic moments of the orientation probability distribution function. This representation was first introduced by Advani and Tucker in the context of short fiber reinforced plastics [17]. Their eigenspace can be used to interpret the orientation direction and the predominant orientation. See Figure 5 where the eigenvalue  $\lambda_3$  is used to describe the preferred orientation.

Depending on the orientation state and the fiber concentration, the cell size can be estimated.

For low concentrations (dilute regime), the following approximation applies regardless of the fiber orientation

$$\frac{h}{R} = \frac{L}{R} \tag{9}$$

with the fiber length  $L$  [18]. For the mean concentration regime,  $h/R$  can be estimated depending on the fiber orientation. Therefore we use the volume fraction  $\phi$  defined as volume of all fibres in the fluid over the volume of the suspension. For uniaxial orientation the following applies

$$\frac{h_{uni}}{R} = \sqrt{\frac{\pi}{\phi}} \tag{10}$$

and for completely random distribution applies [19]

$$\frac{h_{\text{iso}}}{R} = \frac{\pi}{2\phi a_r} \tag{11}$$

Between these two states, Chung and Kwon propose a linear weighting for the mean concentration regime, using the scalar orientation measure  $f_F$  (cf. [21]) as a weighting factor [20], i.e.,

$$\frac{h}{R} = (1 - f_F) \frac{h_{\text{iso}}}{R} + f_F \frac{h_{\text{uni}}}{R} \tag{12}$$

In the high concentration regime, the mean fiber spacing is no longer significantly dependent on the orientation state and  $h/R = h_{\text{uni}}/R$  always applies.

The course of  $h/R$  with respect to the volume fraction is to be evaluated for fibers of slenderness  $a_r = 30$  as was the case in our experimental preliminary work [22]. The fibers used in the previous work are conventional rod-shaped steel fibers with a length of 12 mm, a diameter of 0.4 mm with a scattering range in measurements of max.  $\pm 8\%$ . The concrete composition corresponds to the standard formulation of SPP 1182 [23]. No sedimentation and no influence of fibre bending could be detected in the experiment, so the numerical simulation does not take into account these effects. For the low concentration regime, this results in a volume fraction of  $\phi < 0.09$  vol.-%. In the range of low concentrations, the cell radius can be approximated constantly according to the approximation of Batchelor (cf. Equation (9)) [18]. In the range of medium concentrations ( $0.09 \text{ vol.-%} \leq \phi \leq 2.62 \text{ vol.-%}$ ) the mean fiber spacing and thus also the cell radius  $h$  decreases. In addition, the orientation distribution becomes relevant. The two limiting cases of uniaxial and isotropic fiber distribution are shown in Figure 2 by the limiting curves. In the subsequent highly concentrated regime, the influence of the fiber orientation on the cell radius decreases again and the approximation for uniaxial orientation from the medium concentration regime is continued.

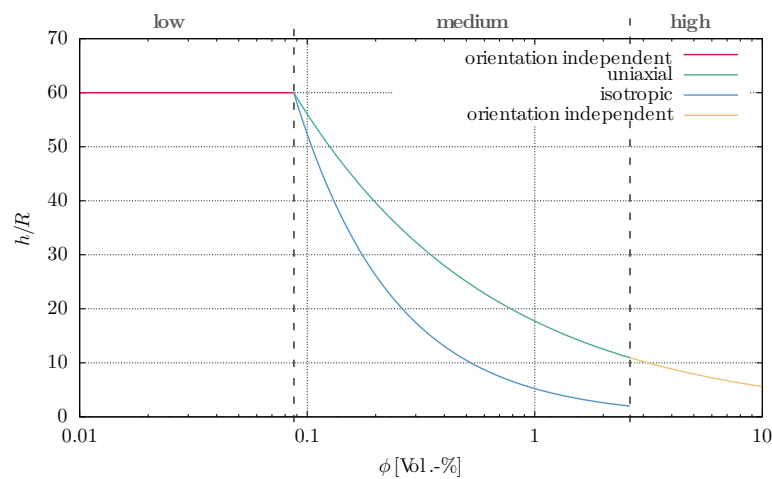


**Figure 2.** Size of the dimensionless cell radius  $h/R$  depending on the fiber volume fraction  $\phi$  and fiber orientation state in the different concentration regimes. In the case shown,  $a_r = 30$ .

It is worth noting, that in this definition, a discontinuity in the approximation of the cell radius is recognizable for anisotropic orientation states. To our knowledge, however, this weakness of the model is an open research question.

Equation (8) is related to the models for Newtonian matrix fluids. The first term corresponds exactly to the formulation for Newtonian matrix fluids [19,20], which is also derived from Slender Body Theory. The second, yield stress-dependent term in Equation (8) has no equivalent in the models for Newtonian matrix fluids. It can be interpreted as a concentration-dependent, anisotropic increase of the yield point in the orientation direction of the fibers. In particular, this term is independent of the shear rate and thus actually has

the character of a yield point. It should be noted that this term also disappears in the case of a vanishing yield point and thus the special case of the Newtonian matrix is implicitly included in the model. For higher local Bingham numbers, i.e., if there is a significant unsheared fluid region within the cell ( $Bm \approx 1$ ) or if the sheared fluid fraction within the cell is even negligible ( $Bm \gg 1$ ), additional terms must be added. For details, please refer to [16].

The orientation-evolution equation was also derived by the authors, whereby the upper-convected derivative of the fiber orientation tensor [16]

$$\overset{\nabla}{\mathbf{A}}_2 = \begin{cases} -2\mathbf{D} : \mathbf{A}_4 + \frac{\tau_y}{\mu} \left( \frac{h/R-1}{a_r} \right) (\mathbf{I} - 3\mathbf{A}_2) & \text{for } |\tau| > \tau_y \\ \mathbf{0} & \text{for } |\tau| \leq \tau_y \end{cases} \quad (13)$$

The special case of a Newtonian matrix fluid is directly recognizable when the yield stress disappears because the equation then corresponds to the Folgar-Tucker equation. The second term, on the other hand, can be interpreted as a correction term compared to the Newtonian solution. It represents a diffusivity of the fiber orientation. *Diffusivity* is not to be understood in the mathematical sense of a diffusion term (in this sense it is a source term), but as a preference for the isotropic orientation state—a preferred orientation is diffused (lat. *diffundere*). The larger this term is or the ratio of yield stress and plastic viscosity is, the greater the reduction in orientation compared to a Newtonian matrix. The modeling of diffusivity of fiber orientation due to fiber-fiber interaction by common models such as isotropic rotary diffusion (IRD) [9], anisotropic rotary diffusion (ARD) [24] or a data-driven diffusion model based on microscale simulations [25] was not used in the investigations within the scope of the present work. In the investigated fiber volume fraction and taking into account the investigated aspect ratio, only a slight influence of the orientation reduction due to hydrodynamic fiber-fiber interaction is to be expected, which would not lead to an increase in accuracy for the study results.

Of particular importance for the applicability of the Equation (8) is the presence of the fourth-level orientation tensor  $\mathbf{A}_4$ , which is approximated in the form of a closure approximation. The closure approximation used in this work is the IBOF-5 closure approximation published by Chung and Kwon [26]. It belongs to the class of invariant based optimal fitting (IBOF) and uses a fifth degree polynomial in the second and third invariants of  $\mathbf{A}_2$ , which represents a good compromise between the computational resources required and the achievable accuracy of the approximation for the orientation tensor of rank four.

## 2.2. Considerations for Estimating the Relative Cell Size

In the experimental investigation of the fiber suspension based on Newtonian silicone oil (Section 1.1), it was shown that the addition of fibers in the medium concentration regime does not cause an (apparent) yield point. In this context, the term *apparent yield point* means that the measured torque-rotational speed relation still shows no yield stress after interpretation as a homogeneous Bingham material.

In addition, a linear increase in torque with the fiber volume fraction was observed. After interpreting the torque-rotational speed relation as a homogeneous fluid (i.e., without modeling the fiber stresses), this also corresponds directly to a linear increase in viscosity with the fiber volume fraction for Newtonian fluids. The fiber constitutive law in Equation (8) assumes the approximation of the dimensionless cell size  $h/R$ . For this purpose, two approximation approaches were presented in Section 2.1 for the limiting cases of isotropic and uniaxial orientation. In the following numerical investigation, the modeling of fiber-fiber interaction by a diffusion model was neglected. The fiber orientation Equation (8) is then independent of the fiber volume fraction. However, there is still a dependence on the fiber volume fraction for the fiber constitutive law. The corresponding term for Newtonian matrix fluid is:

For the Newtonian silicone oil, the yield point  $\tau_y = 0$ , so that the fiber stress term simplifies to Equation (14) and the matrix stress component is Equation (15) with  $\mu$  the dynamic viscosity of the silicon oil. [17]

$$\mathbf{T}^f = \mu\phi \frac{2a_r^2}{3 \ln(h/R)} \mathbf{D} : \mathbf{A}_4 \tag{14}$$

and the extra stress component caused by the matrix is:

$$\mathbf{T}^m = 2\mu \mathbf{D} . \tag{15}$$

The two terms obviously have different relations to the prevailing deformation velocity state. However, the terms  $\mathbf{D} : \mathbf{A}_4$  and  $\mathbf{D}$  do not differ in their order of magnitude, since for each component of the fourth-level orientation tensor  $|A_4^{ij}| \leq 1$  is valid.

$$\phi \frac{2a_r^2}{3 \ln(h/R)} . \tag{16}$$

Special attention should now be paid to the expression  $h/R$ . It describes the relative cell size and is an essential model parameter of slender body theory. The relative cell size depends not only on the fiber volume fraction, but also on the mean local orientation distribution. The estimation of the relative cell size was presented in Equation (9) to Equation (12) for uniaxial and isotropic orientation states. All scalar orientation measures are represent normalized formulations of only one of the two relevant invariants of the orientation tensor, each of which are not linearly related to the character of the orientation state. A linear interpolation based on scalar orientation measures as in Equation (13) does therefore not seem to be a suitable approach. For the following application, the parameter is therefore assumed to be constant in the entire sample for simplicity's sake. A more precise estimation of the relative cell size remains a research question to be investigated in subsequent work. For the fibers used in the experiments in our previous study [3] with  $a_r = 30$ , the expression (16) is shown in Figure 3 for the approximations of the relative cell size.

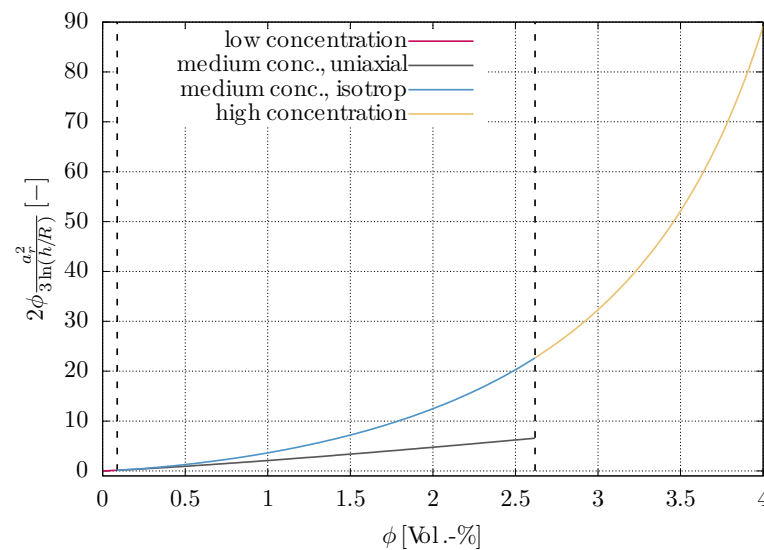


**Figure 3.** Pre-factor of the fiber stress term as a function of fiber volume fraction and orientation state for  $a_r = 30$ .

For the uniaxial orientation state, the function of the pre-factor is linear, while for the isotropic, unoriented state a higher, non-linear slope can be read off.

For the application in the ball probe rheometer, however, the orientation state is locally completely inhomogeneous and, in addition, the flow and orientation direction

as well as the flow type (elongation, shear) differ significantly in large regions. In the relevant concentration range, however, it can be assumed that the orientation state is mainly dominated by the flow type of the matrix and not by the constitutive effect of the fiber concentration itself. The measurement results presented in [3] showed that when interpreted as a homogeneous substitute fluid, both Binghamian and Newtonian fluids show a linear increase in viscosity (without change or build-up of yield stress) at least in the medium concentration regime. In light of this, Figure 3 shows that at least in the near field around the ball probes, which is relevant for the torque, a predominantly uniaxial orientation state must be present in order to explain the linear slope of the relative viscosity with the fiber volume fraction.

### 2.3. Interim Conclusion

The previous consideration for estimating the relative cell size suggests that the linear relationship between relative viscosity increase and fiber volume fraction determined in the experiment can (rather) be described by the approximation approach for uniaxial orientation states. However, this conflicts with our finding from [2] that the orientation process is extended over a period of time that corresponds to the usual measurement duration. It was also observed in the experimental investigations that rapid orientation processes only take place near the ball probe, i.e., in regions with strong shear. In order to come closer to answering the question of how the relative cell size can be formulated as a model parameter, some of the experiments are to be reproduced numerically. For this reason, a comparison between numerical simulation results and the quantities determined in the experiment will be carried out below using the example of the suspension with 2 vol.-% fibers. For this purpose, the experiment is numerically simulated twice, whereby the relative cell size is chosen to be spatially constant and temporally invariant in each case using the two approximation approaches.

## 3. Results

### 3.1. Numerical Setup

For the numerical investigations, the flow of the suspension based on the Newtonian silicone oil is solved in the Schleibinger eBT2 ball probe rheometer on the same mesh as presented in [1]. For that reason, in the present study, we refer to the preliminary investigations for validation in the referenced article. A significant difference, however, is that a steady-state solution method cannot be used for the following investigations. A non-stationary solution is necessary because the fiber orientation changes over time and is dependent on its history.

The velocity and pressure boundary conditions remain unchanged, whereby the progression over time of the rotational velocity ramp of the ball probes corresponds to the experiments in our previous studies [1,3]).

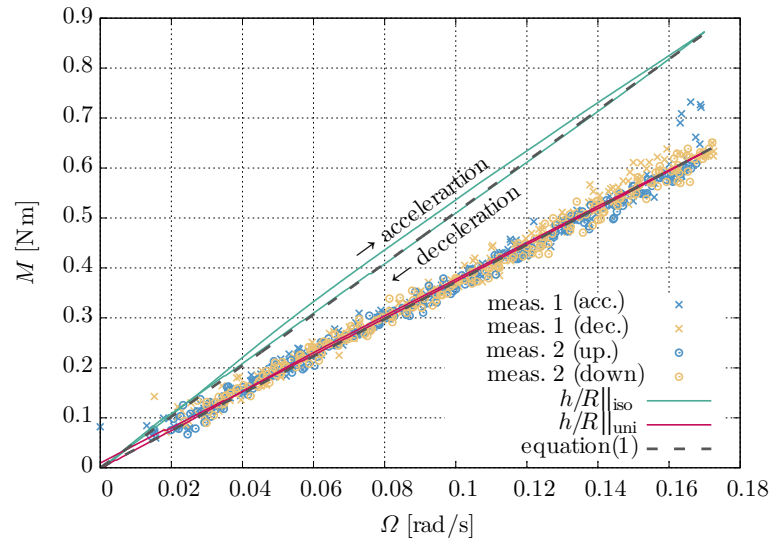
$$\Omega_a(t) = \begin{cases} \frac{0.17 \text{ rad}}{32.8 \text{ s}} t; & t \leq 32.8 \text{ s} \\ 0.17 \text{ rad} - \frac{0.17 \text{ rad}}{32.8 \text{ s}} (t - 32.8 \text{ s}); & \text{else.} \end{cases} \quad (17)$$

The uniaxial orientation state ( $\mathbf{A}_2 = 1/3\mathbf{I}$ ) was set for the initial orientation in the entire domain. This also corresponds to the initial state aimed for in the experiments. In practice, this state could not always be ensured locally. This deviation from the experimental results must be taken into account when interpreting and evaluating the numerical results. The material parameters of the matrix fluid ( $\eta = 111.7 \text{ Pa s}$ ;  $\rho = 970 \text{ kg m}^{-3}$ ) were set according to the measurements presented in our previous study.

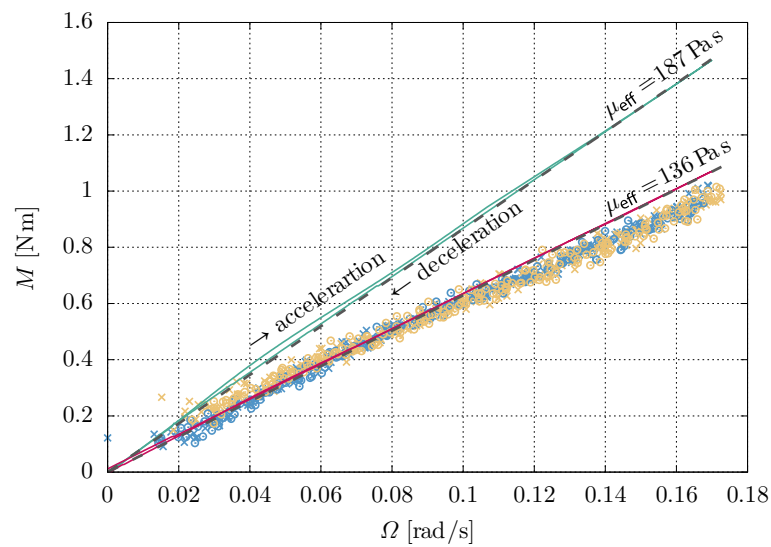
On both ball probes, the resulting torque around the axis of rotation was calculated from the integration of the total fluid stresses over the surface of the sphere,

$$M_K = \iint_{A_K} \left\{ \left[ -p(\mathbf{x})\mathbf{I} + \mathbf{T}^f(\mathbf{x}) + \mathbf{T}^m(\mathbf{x}) \right] \cdot \mathbf{n}(\mathbf{x}) \right\} \times \mathbf{r}(\mathbf{x}) \, dA \quad (18)$$

where  $r(x) = x - x_0$  describes the distance between the coordinate origin  $x_0$  on the axis of rotation at the bottom of the container and the location  $x$  on the surface of the sphere.  $n(x)$  is the wall normal vektor. The torque for the two simulations with  $h/R|_{iso}$  and  $h/R|_{uni}$ , as well as the torque determined in the experiments, is shown for both ball probes in Figure 4.



(a) MK105



(b) MK145

**Figure 4.** Torque-rotational speed correlation on the ball probes MK105 (a) and MK145 (b) of the eBT2. The experimental data (symbols), the simulation results (lines) and the Equation (1) (homogeneous replacement fluid, dashed lines) adapted to the simulation results based on the dynamic viscosity are shown.

For both cell size approximations, an approximate linear torque-rotational speed curve can be seen in both the upward and downward curves. The curves can be described by the torque-rotational speed relation (1) drawn as a dashed line. When interpreted as homogenous fluid, this results in a Newtonian fluid with the effective viscosity  $\mu_{eff}$  of 136 Pa·s under uniaxial cell size approximation or 187 Pa·s under isotropic cell size approximation. (Effective viscosity is also known as apparent viscosity. In this paper we use the term effective viscosity.) As expected from the estimates in connection with Figure 3, the torque is higher under the isotropic cell size approximation at any rotational speed than under the uniaxial approximation, depending on the rotational speed by 37.5%.

This difference is significantly smaller than the ratio of the fiber stress pre-factors (163% at 2 vol.-%), because this term only relates the fiber stresses and, unlike the torque, does not take into account the larger fluid stress component. Regardless of the cell size estimation approach, there is a slight hysteresis of the torques between the upward and downward curves, whereby the absolute difference with  $h/R|_{\text{iso}}$  is more significant than with  $h/R|_{\text{uni}}$ . In both cases, the width of the hysteresis is smaller than the scatter of the measured values in the experiment. From the low hysteresis, it must be concluded that, unlike in the Couette flow, the orientation process only slightly influences the flow in the ball probe rheometer, at least in the vicinity of the ball probes. The orientation development will be examined in more detail later in order to better understand this difference to the Couette flow.

It is noticeable that the curves of both probes recorded in the experiment are in good agreement with the numerically determined curves for the uniaxial cell size approximation. In the experiment, both measurements consistently recorded a drop in the curve gradient at MK145 in the range of higher rotational speeds ( $\Omega > 0.1$  rad/s) in both the upward and downward curves. This effect does not occur in any of the simulations. However, the effect is also not observed in any of the measurements with a similar fiber volume fraction ( $1 \text{ vol.-%} \leq \phi \leq 3 \text{ vol.-%}$ ), so that a random scattering effect in the repeat measurements must be assumed rather than an insufficient description by the orientation model. With regard to the above-mentioned discussion about the linear relationship between effective viscosity and fiber volume fraction, this observation strengthens the hypothesis that the estimation with uniaxial orientation is suitable for the approximation of the cell size for the investigated flow.

Figure 5 shows the temporal development of the fiber orientation state during the measurement process with ramp profile. The three-dimensional isocontour is shown, for which the largest eigenvalue has the value 0.8. The color of the contour surface also indicates where there is an even clearer preferred orientation. Regardless of the direction in which the preferred orientation is present, it can be seen that after 20 s or after about 1/5 rotation (cf. Figure 5c), there is an almost uniaxial orientation ( $\lambda_3 \rightarrow 1$ ) on the ball probe (MK145) located further out directly on the wall of the probe. With increasing time, the range of uniaxial fiber orientation on the outside of the sphere increases and a uniaxial fiber orientation can also be seen on the ball probe (MK105) located further inside. However, it is noticeable that the preferred orientation is only present on the outer half of the sphere for both ball probes. On both ball probes, the orientation state near the ball on the inside of the trajectory is  $\lambda_3 < 0.8$  until the end of the process. The main reason for this is the significantly lower shear rate on the inside of the sphere. The shear rate distribution in the field is examined in more detail later in the chapter. It can also be seen that the fiber orientation state is transported convectively. As expected, the fibers on both sphere probes initially begin to adopt a preferred orientation between the sphere and the bottom of the container. The highest shear is to be expected in this region because this is where there is the smallest distance between two walls moving relative to each other.

As the rotational speed of the ball probes increases, the shear on the outside of the sphere also increases and begins to influence the fiber orientation there. The already pre-oriented fibers then move approximately along the respective probe orbit. Because the shear rate is higher at the outer ball probe MK145 than at the probe MK105, not only fibers close to the ground are oriented there. Therefore, the isocontour, which shows the trailing of the MK145 probe, is about the same length over the entire sample height, while the isocontour in the trailing of MK105 is very pointed near the ground. After around half a rotation (35 s), the fibers in the trailing edge of the inner ball probe MK105 reach the area of influence of the outer ball probe. There they are mainly moved past the inner side of the ball probe. The fibers from the trailing end of MK145, on the other hand, move past the outer side of MK105 and are pushed towards the outer wall of the container in the area of influence of MK105, so that two orientation bands are initially created (cf. Figure 5g), which merge as the process continues. At the end of the process (cf. Figure 5j), it is clearly

recognizable that a uniaxial preferred orientation is only present in a few places at the edge of the container.

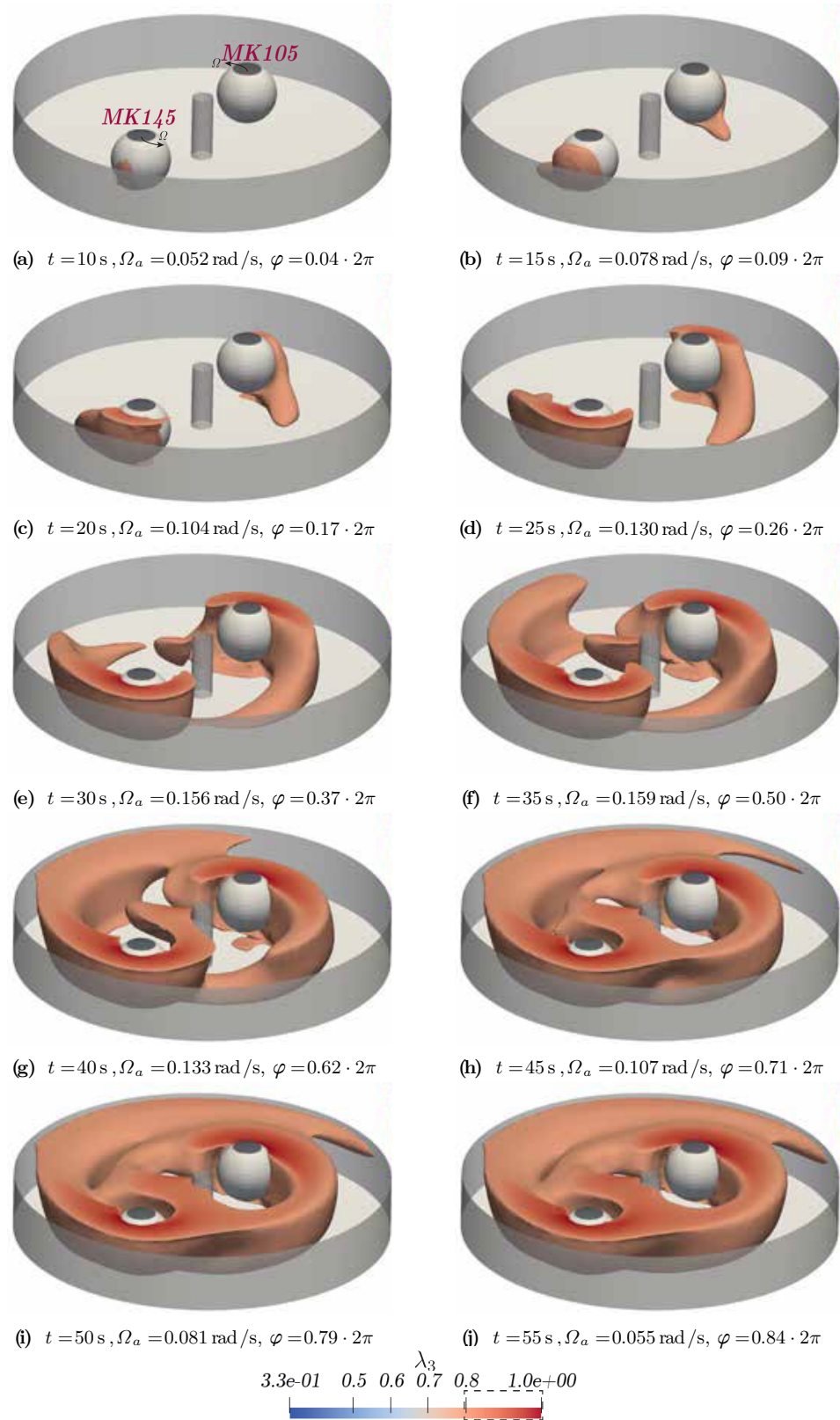


**Figure 5.** Development of the preferred orientation during the process ( $h/R||_{\text{uni}}$ ). The largest eigenvalue  $\lambda_3$  of the orientation tensor  $\mathbf{A}_2$  is shown both in the color coding and with the isocontour for  $\lambda_3 = 0.8$ .  $\Omega_a = -\Omega_{\text{sphere}}$ .

The torque-rotational speed curves in Figure 4 showed only slight hysteresis between the upward and downward curves. Although the torque provides information about the stress and thus indirectly about the flow state on the ball probe surface, it does not necessarily provide information about the flow state in the overall domain. In connection with Figure 5, the development of a preferred orientation could be illustrated. The orientation process extends over the entire duration of the measurement. The local direction of the preferred orientation and its possible influence on the flow field is shown in Figure 6. The figure shows the streamlines in the moving reference frame rotating with the ball probes at the same rotational speed (0.08 rad/s) in the upward (Figure 6a) and in the downward curve (Figure 6b). Based on the streamlines and the shear rate represented by their color, no significant difference can be detected in the overall field either. This result confirms the torque investigations and leads to the conclusion that the temporal, global development of the fiber orientation is negligible with regard to its influence on the flow in the ball probe rheometer, although the process extends over the entire measurement period.

The orientation ellipsoids give a visual representation of the relations between the three eigenvalues of the orientation tensor. Therefore the orientation ellipsoids show the development of the preferred orientation direction over the entire process. As can already be seen from Figure 5, the formation of the preferred orientation only takes place in the immediate vicinity of the outer sides of the ball probes. It is transported from there almost unchanged on circular paths. The orientation angle relative to the streamline remains almost unchanged. This is to be expected because the shear rate drops rapidly far away from the ball probes, meaning that the suspension follows a rigid body rotation there. The direction of orientation in the spherical oncoming flow follows the compression movement of the fluid, so that the fibers in the spherical oncoming flow are aligned approximately perpendicular to the streamlines. In the near field of the outside of the sphere, the fibers, which are already subject to a preferred direction, then rotate in the tangential direction of the spheres and achieve a preferred direction almost tangential to the streamline in the wake flow of the sphere. The further away the streamlines (and the fibers following the fluid) pass the surface of the ball, the less their direction of orientation follows the contour of the ball, so that the orientation remains perpendicular to the streamline.

There are no systematic measurements or records of the orientation of the fibers in the experiment. The comparison with the photographs in [2] at least allow a qualitative comparison. In the oncoming as well as in the wake flow of both ball probes, the preferred orientation determined in the simulation agrees well with that documented in the experiment.

In Figure 5, an extensive region can be seen on the inside of MK105 in which no (uniaxial) preferential orientation is achieved. This region corresponds to the inner vortex also recognizable in Figure 6 on the basis of the streamlines.

However, the orientation state on the outer side of the trajectory of the ball probe does not seem to match the experiment in the simulation. There are two possible reasons for this: On the one hand, while preparing the experiments the direction of the stirring and thus the resulting fiber orientation could already have been tangential to the container wall due to the manual mixing and filling process. In the simulation, however, an ideally isotropic orientation was assumed as the initial condition for the entire domain. On the other hand, the shear rate drops very quickly in the probe normal direction. The fibers used in the experiment have a length of 12 mm. The orientation model assumes that the velocity gradient is constant over the fiber length. This condition is therefore not fulfilled in the vicinity of the balls. In addition, the fiber orientation model does not take into account wall contacts and the associated forced orientation of the fibers tangential to the container wall. This can explain the difference between experimentally and simulatively determined fiber orientation, especially in the area of the container wall, because unlike at the ball probes, shear-induced fiber orientation only occurs to a small extent there. In future experimental studies, the orientation of the fibers in this area should be investigated in more detail in order to clarify the discrepancy between simulation and experiment.

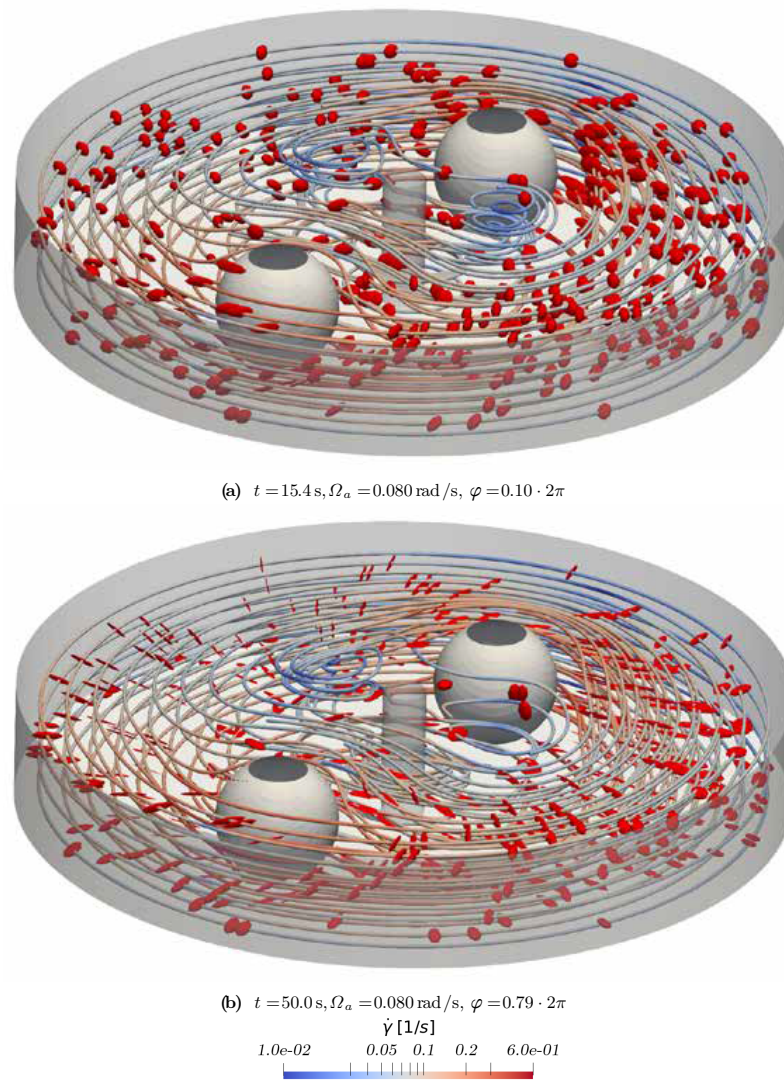


**Figure 6.** Orientation ellipsoids and streamlines at the same rotational speed  $\Omega_a = 0.08 \text{ rad/s}$  in the (a) acceleration and (b) deceleration curve ( $h/R_{\text{uni}}$ ). The streamlines are colored with the local representative shear rate  $\dot{\gamma}$ .

### 3.2. Inertia of the Matrix Fluid

The time scales in which the inertia of the fluid is overcome and in which a stationary orientation of the fibers in the rheometer is established differ significantly. For this reason, the duration after which the matrix fluid has overcome the start-up process is estimated again for the flow in the concrete Rheometer.

For a plane channel startup flow, the dimensionless time

$$\tilde{t} = \frac{\mu t}{\rho H^2} \tag{19}$$

with channel height  $H$  of the couette cell can be related to the startup process, as steady-state is reached for  $\tilde{t} > 0.5$ . For the ball probe rheometer, with

$$\tilde{t} = \frac{\mu t}{\rho D_k^2} \tag{20}$$

a similar dimensionless time formulation can be found.

Taking into account the viscosity of the silicone oil and the ball diameter and assuming that  $\tilde{t}_{\text{stat}} \geq 0.5$  also applies in the concrete rheometer, the fluid inertia is already overcome

after  $t_{\text{stat}} \geq 0.0277$  s. An influence of inertia can therefore be ruled out in all measurements. It should be noted that Equation (20) used for estimation can only be expected to have limited accuracy for this application because the flow state is significantly more complex than that of the channel flow. However, the order of magnitude of well under a tenth of a second is sufficiently reliable to separate the time scales of inertial effects and the orientation process.

### 3.3. Investigations at Constant Rotational Speed

The Couette flow investigated in [2] shows a clearly time-dependent torque development, which directly follows the low fiber orientation dynamics. Although an orientation process lasting over the measurement procedure was also identified in the ball probe rheometer, the torque essentially follows the rotational speed without significant hysteresis in the ramp. In the ramp profile, however, the development of the fiber stresses overlaps with the increase in fluid stresses due to increasing rotational speed. In order to investigate the influence of the orientation dynamics on the torque in isolation, further numerical investigations are now to follow at a constant rotational speed ( $\Omega_a = 0.17$  rad/s) over a process duration of 60 s or 1.6 revolutions.

The orientation development in Figure 5 already showed in the investigations on the ramp profile that the steady-state orientation is quickly reached in the immediate vicinity of the ball probes in the region of high shear rates. Figure 7 shows the development of the torque over the dimensionless time  $\tilde{t}$  (cf. Equation (20)) at  $\phi = 2.0$  vol.-% and constant rotational speed for both ball probes. The cell size approximation for uniaxial orientation is used for this and the following investigations. At both ball probes, an increase in the torque can be read immediately at the beginning of the process up to about  $\tilde{t} < 100$ . The increase is 6 % compared to the steady-state torque ( $\tilde{t} > 900$ ) at MK105 and 4 % at MK145. The torque also shown, which is achieved in the ramp profile at the same rotational speed, does not differ from the stationary torque in these investigations. The torque increases on both ball probes by 20 to 24 % compared to the fiber-free matrix fluid.

An influence of the orientation dynamics is therefore mainly limited to the startup process, which for  $\phi = 2$  vol.-% is essentially already completed at  $\tilde{t} > 100$ . In a further investigation, the fiber volume fraction was reduced to 0.674 vol.-%. The torque curve is shown in Figure 8.

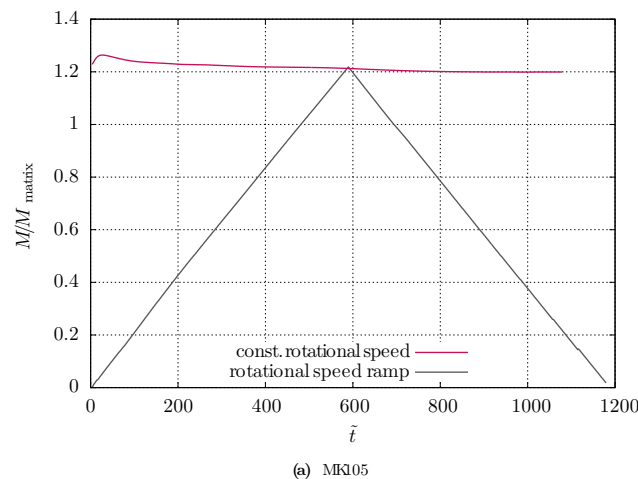
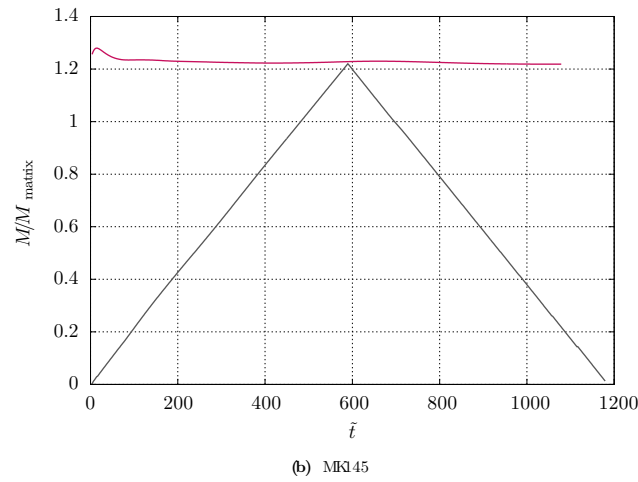
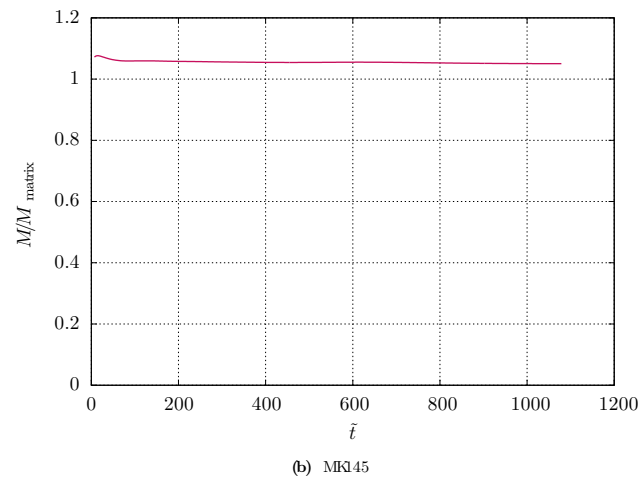
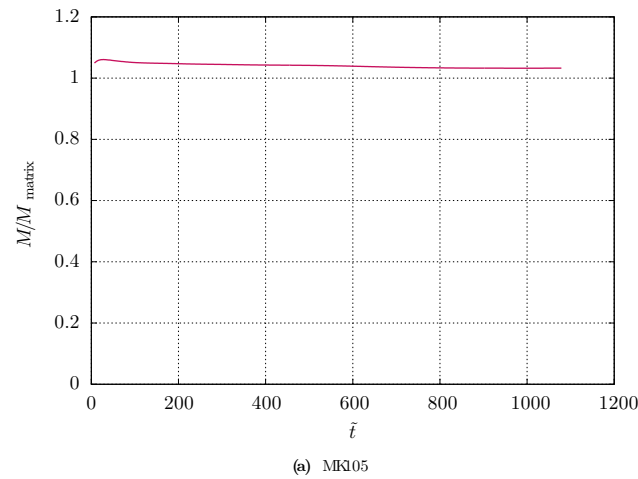


Figure 7. Cont.



**Figure 7.** Development of the torque calculated in the simulation of the fiber suspension ( $\phi = 2.0$  vol.-%) in relation to the fiber-free Newtonian matrix fluid ( $\mu = 111.6$  Pa s) on both ball probes of the eBT2 (comparison of constant rotational speed ( $\Omega_a = 0.17$  rad/s) with torque ramp as in the experiment).



**Figure 8.** Development of the torque calculated in the simulation of the fiber suspension ( $\phi = 0.674$  vol.-%) in relation to the fiber-free Newtonian matrix fluid ( $\mu = 111.6$  Pa s) on both ball probes of the eBT2 (comparison of constant rotational speed ( $\Omega_a = 0.17$  rad/s) with torque ramp as in the experiment).

Here, there is also a slight torque overshoot in the startup phase. As the fiber content decreases, the extent of the torque boost also decreases.

The characteristic torque increase, which can be observed at the beginning of the process at a constant rotational speed, has also been documented for other types of concrete

rheometers. In vane rheometers, in which a spatially inhomogeneous flow field is also present as in ball probe rheometers, a comparable orientation-induced torque increase could be observed [7]. The referenced example in Figure 9 shows the temporal development of the torque of a cement mortar sample in a vane rheometer without specifying the fiber content and fiber geometry. Here, an torque overshoot of 22 % was observed compared to the steady-state torque.

Since the present investigations involve a Newtonian matrix fluid, it is also possible to determine the effective viscosity of the suspension from the simulations with a constant rotational speed.

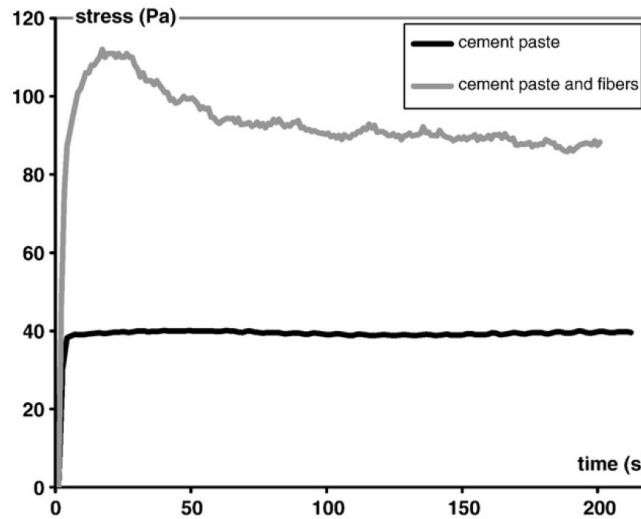


**Figure 9.** Measurement of the shear stress of a cement mortar with and without the addition of fibers in a paddle rheometer (*vane rheometer*). The source contains no information about the fiber geometry and the fiber volume fraction [7].

In [1] it was shown that the dimensionless torque  $\Pi_1$  is constant for Newtonian fluids. This means that the dimensional torque is linearly proportional to the effective dynamic viscosity of the suspension.

The relative viscosity increase determined for the two numerically investigated fiber concentrations compared to the experimentally determined values can be found in Figure 10.

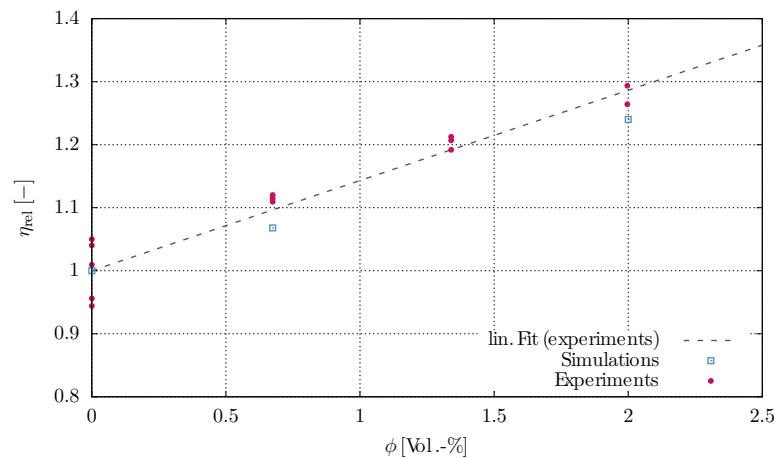


**Figure 10.** Relative effective viscosity of the Newtonian fiber suspension over fiber volume fraction. Comparison between numerical simulation and experiment.

The values determined from the simulations are lower than the experimentally determined values for the same fiber concentration, but the deviation is in the order of magnitude of the scatter of the experiments.

The torque is an integral quantity. According to Equation (1), a Newtonian fluid with a viscosity of 134 Pa s generates the same torque on both spheres as the suspension with  $\phi = 2.0$  vol.-% in the steady state. The determination of the equivalent viscosity in the investigations on the ramp profile resulted in the value 136 Pa s. The slight deviation of 1.5 % can be explained with the help of Figure 7 by the fact that the orientation process in the ramp profile is not yet fully completed when passing through the rotational speed  $\Omega_a = 0.17$  rad/s. The application of this evaluation rule under the assumption of an effective Bingham or Newtonian behavior of the fiber suspension implicitly assumes that the flow behavior not only locally at the ball probes, but in the overall field corresponds to the flow behavior of the fictionally homogenous substitute liquid with the same effective properties. To check the validity of this hypothesis, Figure 11 shows a comparison of the shear rate fields of the suspension with  $\phi = 2.0$  vol.-% after reaching the steady-state torque and a Newtonian substitute fluid with the viscosity 134 Pa s.

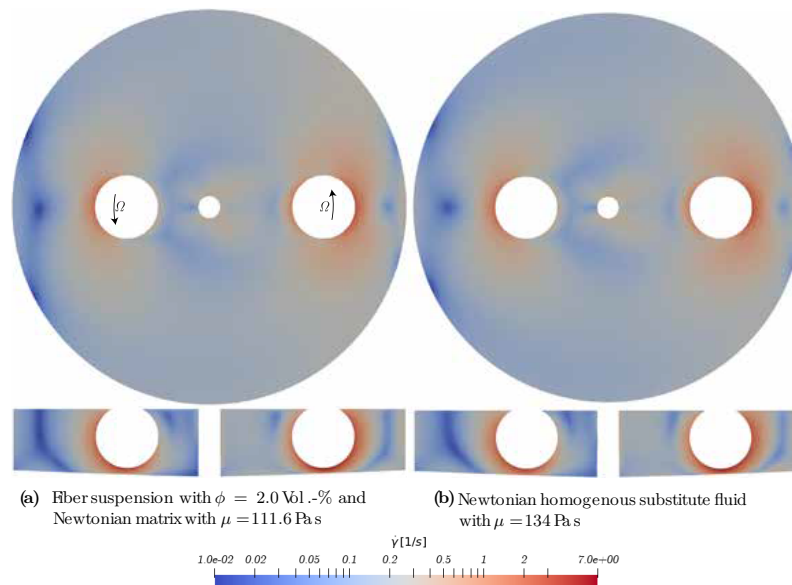


**Figure 11.** Field of the equivalent shear rate in comparison between the fiber suspension (a) and a Newtonian substitute fluid (b), which produce an identical torque on the spheres.

In the shear rate fields in two views through the ball probes, it can be seen that the two modeling approaches also show locally consistent results in wide areas. The areas of higher and medium shear rates are indistinguishable both in terms of magnitude and quality. Only the very low shear rates are even lower in the modeling with the fiber model. However, areas with low shear rates do not have a significant effect on the velocity and pressure field anyway, so this difference is negligible. It can therefore be stated that a description as a fiber-free substitute fluid also describes the local flow field of the fiber suspension in the ball rheometer very well.

Finally, the orientation dynamics at different points in the sample container will be investigated. They are presented in Figure 12 and Table 1.

Figure 13 shows the development of the orientation in the immediate vicinity of the ball probes, in each case at a point directly in the upstream and downstream flow, as well as on the outside and inside of the trajectory and in each case at a position in the more distant wake of the spheres. Both spheres show the particularly rapid setting of a preferred orientation on the outside of the trajectory, i.e., in the region of high shear, which can already be seen at the maximum torque overshoot at  $\tilde{t} \approx 25$  is already  $\lambda_3 > 0.6$  (MK105) resp.  $> 0.7$  (MK145).

**Table 1.** Coordinates of the observation points in the spherical equatorial plane. The origin of the coordinates lies on the axis of rotation.

| Ball Probe | No. | Description    | Position [m]     |
|------------|-----|----------------|------------------|
| MK105      | 1   | Oncoming flow  | (−0.105; −0.047) |
|            | 2   | Wake flow      | (−0.105; 0.047)  |
|            | 3   | Outside        | (−0.15; 0)       |
|            | 4   | Inside         | (−0.06; 0)       |
|            | 5   | Far field wake | (0; 0.145)       |
| MK145      | 6   | Oncoming flow  | (0.145; 0.047)   |
|            | 7   | Wake flow      | (0.145; −0.047)  |
|            | 8   | Outside        | (0.19; 0)        |
|            | 9   | Inside         | (−0.1; 0)        |
|            | 10  | Far field wake | (0; −0.185)      |

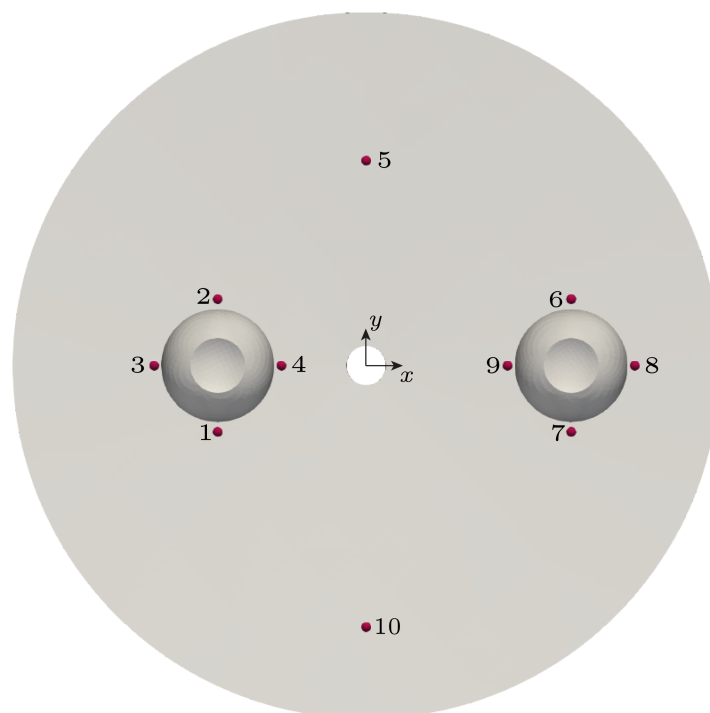


**Figure 12.** Observation points for the orientation state in the spherical equatorial plane.

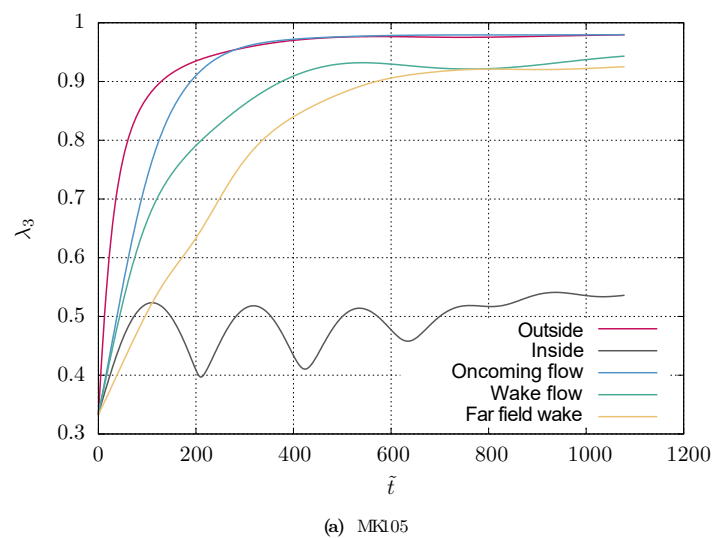


**Figure 13.** Cont.

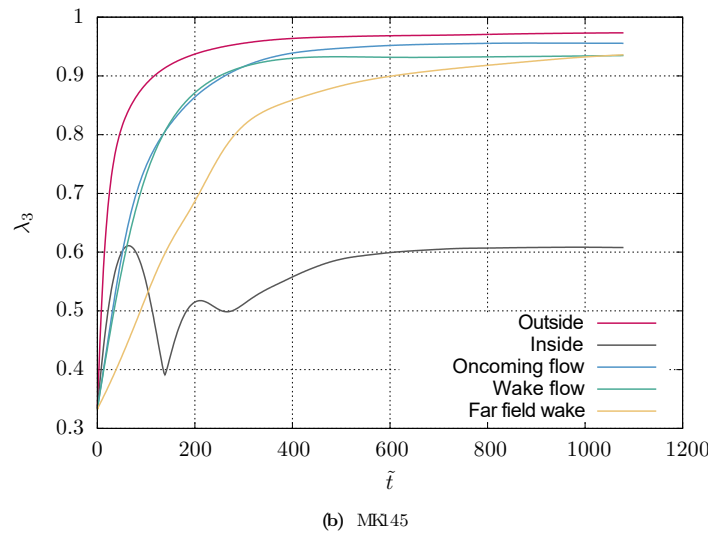


**Figure 13.** Evolution of the largest eigenvalue  $\lambda_3$  of the orientation tensor  $\mathbf{A}_2$  at selected observation points around the ball probes of eBT2. Constant rotational speed  $\Omega_a = 0.17$  rad/s,  $\phi = 2$  vol.-%,  $\mu_{\text{matrix}} = 111.6$  Pa s.

The orientation development on the inside of the orbit is not monotonic on both spheres, but oscillates. At MK145 it reaches a steady-state after  $\tilde{t} > 700$ , at MK105 only after  $\tilde{t} > 900$ , whereby the maximum value of  $\lambda_3$  is in the range 0.54–0.61 in both cases and there is an almost flat, spherical surface-parallel stationary orientation state. The orientation at the oncoming flow and the wake flow takes place at MK145 at a comparable rate. At MK105, on the other hand, the orientation in the wake flow develops much more slowly, but finally reaches the value  $\lambda_3 = 0.94$  at both probes. The significant delay in the orientation development far from the probes can be seen at the additionally investigated point in the far wake of the ball probes. There, the degree of orientation increases much more slowly and is not yet stationary at the end of the simulation.

Figure 13 shows that the orientation of the fibers near the sphere probe starts at a high rate, so that a preferred orientation is formed quickly. The orientation rate then decreases, which is why the stationary orientation state is only reached after a delay. This can also be seen in the temporal development of the torque in Figure 7, as the torque slowly decreases during the process, at least at MK105, even after the end of the camber.

The negligible influence of the orientation state on the velocity field is confirmed by Figure 14. Although the orientation ellipsoids clearly document the development of the orientation state with increasing process duration, the streamline image does not change. However, slight changes occur in the size of the expansion and compression regions. On the inside of the trajectory of MK145, the region with dominant strain (red) becomes more compressed. In the outer region of the trajectory of MK105 close to the container wall, there are also more pronounced expansion and compression states. However, their significance for the orientation formation is low against the background of the overall low shear rates in this region (cf. Figure 11) with

$$Z = \frac{I_3^D}{(-I_2^D)^{3/2}} \tag{21}$$

Equation (21) a dimensionless parameter can be defined, which allows a clear distinction between characteristic flow states for incompressible flows. For  $Z$  the following applies

$$Z = \begin{cases} \frac{2}{2\sqrt{3}}, & \text{uniaxial flow} \\ -\frac{2}{2\sqrt{3}}, & \text{equibiaxial strain flow} \\ 0, & \text{planar expansion flow or shear flow.} \end{cases} \quad (22)$$

It can be seen on both ball probes that the orientation is significantly adjusted on the respective outer side of the path, as already discussed in the context of the simulations with ramp profile. In combination with the shear rate field (Figure 11) and the flow state index  $Z$ , the development of the preferred orientation becomes understandable: When the suspension moves towards the ball probe (wake flow of both ball probes), the suspension is located in areas with pronounced compression ( $Z < 0$ , blue areas in Figure 14), so that a preferred orientation develops perpendicular to the streamline.

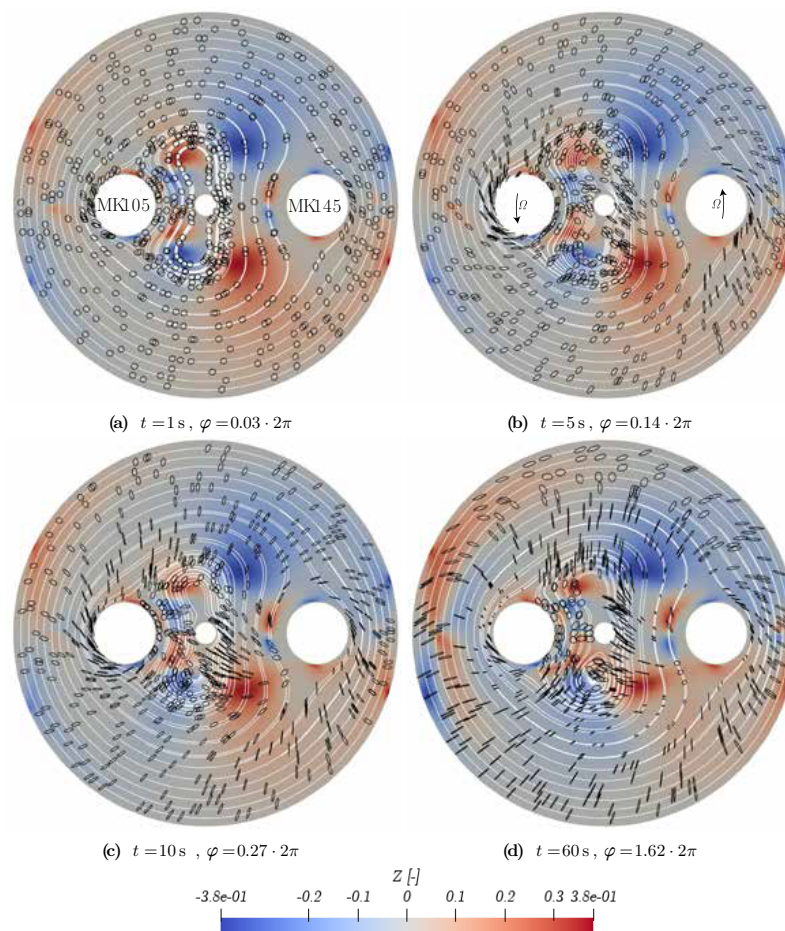


**Figure 14.** Development of the preferred orientation at constant rotational speed  $\Omega_a = 0.17$  rad/s,  $h/R|_{\text{uni}}$  and  $\phi = 2$  vol.-% in the Newtonian matrix fluid in the section through the ball probe equator. Streamlines and flow state index  $Z$ .

On the respective outer side of the trajectory, a significantly smaller domain with dominant shear ( $Z \approx 0$ , gray area) follows at the level of the ball probe center, which causes the orientation ellipsoids, which were previously aligned perpendicular to the streamline, to rotate more parallel to the streamline. Further downstream, i.e., in the area of the spherical flow, the suspension undergoes elongation ( $Z > 0$ , red area), which also causes the orientation ellipsoids to be aligned parallel to the streamline. Unlike in the spherical oncoming flow, however, there is now already a strong preferential orientation and the fibers have already passed the region of greatest shear rates on the outside of the

path, so that the additional orientation effect in the wake flow of the probe is significantly weaker than in the wake flow of both ball probes.

The influence of the elongation, shear and compression regions on the preferred orientation relative to the streamline can also be clearly seen in the vortex region on the inside of the sphere. On the inside of MK145, the fibers initially pass through an area of dominant compression in which they are oriented almost perpendicular to the streamline.

This is followed downstream at the level of the ball probe by a smaller region with dominant elongation, which allows the pre-oriented fibers to rotate parallel to the streamline. This is immediately followed by an area with rather undefined, changing flow conditions, in which the preferred orientation even decreases as is represented by the ellipsoids becoming more spherical again.

In general, it can also be observed that the strength of the preferred orientation initially decreases (or the width of the orientation distribution increases) when passing from stretching to compression regions before a new preferred orientation perpendicular to the streamline is established, while in the opposite case from compression to stretching, the strength of the preferred orientation does not decrease, but only a rotation in the direction parallel to the streamline can be observed.

In the regions where the scalar shear rate is particularly small, the orientation states are transported downstream essentially unchanged both in the width of the orientation distribution (i.e., in the shape of the ellipsoids) and in their angle relative to the streamline.

#### 4. Conclusions and Outlook

In this article, the flow of a fiber suspension in a ball probe rheometer was investigated numerically and compared to the experimental measurement results from [22]. As in the numerical investigation of the Couette geometry in [2], it was also proven in the ball probe rheometer that the fluid inertia is already overcome before the fiber orientation process begins recognizably.

The main results of the work are:

- The experimental investigations indicated that the orientation process of the fibers during the measurements has no influence on the measured torque, because no hysteresis of the torque-rotational speed curves can be detected. The simulation results in this section did show a slight increase in torque during the start-up phase. However, this is smaller than the width of the scatter in the experiment and thus explains the observation that no orientation influence on the measured torque is recognizable.
- The torque at the ball probes is primarily determined by the orientation state at the surface of the sphere and only in areas with a high shear rate. Such areas are located on the outside and underside of the ball probe. At these locations, a clear preferred orientation and a steady-state of orientation is established very quickly. Far away from the ball probes, on the other hand, the orientation process is significantly slower and even lasts longer than the measurement duration selected in the experiment. The orientation tendency could be identified depending on the prevailing flow form. The same effects could also be observed in the flow in the ball probe rheometer (cf. argumentation around Figure 14), whereby the complex succession of flow states causes a less clear and, above all, spatially inhomogeneous orientation distribution in the ball probe rheometer.
- The orientation model requires an approximation of the so-called cell size, i.e., an effective interaction area around a fiber. Based on the cell size approximation for the two extreme orientation states (isotropic vs. uniaxial), the flow was simulated and a comparison of the torques with the experimental results was carried out. It was found that when the cell size approximation for uniaxial orientation states is selected, the experimentally determined torque can be reproduced well, whereas when the approximation for isotropic orientation is used, a significant overestimation of the torque is calculated. This can be explained after analyzing the flow: The cell size approximation is considered in the fiber constitutive law, but not in the orientation-

evolution equation for Newtonian fluids. The term influences the solution in regions with large velocity gradients. In the ball probe rheometer flow, this applies to the vicinity of the sphere, where a uniaxial orientation state dominates particularly quickly. Far away from the ball probes, there is generally no uniaxial orientation. However, due to the low shear rates in these regions, the model error in the fiber constitutive law hardly affects the flow solution due to the uniaxial cell size approximation.

- The simulation model provides a linear increase in the effective viscosity with increasing fiber volume fraction compared to the matrix liquid, whereby the gradient corresponds to the experimental results. Furthermore, the shear rate in the flow field of the suspension was compared with a homogeneous Newtonian substitute fluid, which produces the same torque at the ball probes. No significant differences were found, so that a good approximation can be assumed not only in the integral measured variables, but also locally using a homogeneous substitute fluid.
- In order to investigate the influence of orientation on the torque in more detail and to enable an objective comparison with the previous Couette investigations, additional simulations were carried out at a constant rotational speed. The influence of the orientation process is shown by an increase in torque during the start-up process. A similar characteristic increase at constant rotational speed is also described in the literature for other concrete rheometer geometries such as the vane rheometer. The extent of the torque overshoot increases with increasing fiber volume fraction.

The experimental data on fiber orientation and its development over time is insufficient to carry out a comprehensive comparison with the simulation results. The few existing experimental observations suggest, however, that there is a good agreement of the predicted orientation development near the ball probe, while the model predicts a less clear orientation at the container walls. There are two possible reasons for this, which are not necessarily mutually exclusive: In the numerical simulations, an isotropic initial distribution of the fibers was assumed. In the experiment, this could not be achieved near the wall because the way the fibers were mixed in with a stirring rod prevented this. Furthermore, the orientation model takes into account flow-induced orientation near the wall, but no forced orientation of the fibers due to wall contact. The influence of wall contact is negligible in many applications (e.g., pipe flow) because shear near the wall already represents the orientation development sufficiently well. However, in low-shear or low-distortion regions such as near the container wall, the forced orientation due to fiber-wall contact could have a significant influence on the orientation process. This must be investigated in more detail in future experimental studies.

Thus, the study shows a good representation of the fiber orientation from the experiments. Nevertheless, the numerical model has limitations:

- The model assumes inflexible fibers. Fibers can only be considered inflexible if their deformation does not result in a significant change in the flow around them with the matrix fluid. This usually applies to steel fibers, but generally not to textile fibers, and in particular for polymer fibers this must be examined more closely in individual cases before the model is used.
- The model assumes a homogeneous fiber distribution.
- The model (without extension) does not take into account fiber-fiber interaction, which occurs at higher fiber concentrations. In this case in particular, increased fiber agglomeration can also occur, which results in segregation of the fiber suspension.
- No fiber-wall interaction is taken into account.

There is a particular need for further research into fiber-wall interaction: fiber-wall interaction must be taken into account in flow scenarios where only low shear rates, i.e., a slow flow velocity close to the wall, prevail in flow regions relevant to the investigation. In order to consider fiber-wall effects at low shear rates by model extension in the future, further microscopic investigations are necessary. These could be investigated numerically by microscale approaches, for example with CFD-DEM, or experimentally by simultaneous measurement of the near-wall flow profiles (for example with PIV) and optical identification

of the time-resolved fiber orientation process, which requires a transparent matrix fluid and thus a substitute fluid for the fresh concrete.

Similarly, model extensions could take into account the fiber-grain interaction and the resulting reduced orientation tendency in fresh concretes with a higher aggregate content. In this case, too, the microscale investigations required for modeling could be determined using microscale simulations or experimentally.

**Author Contributions:** Conceptualization, F.G. and T.S.; methodology, F.G. and O.W.; software, F.G. and T.V.; writing—original draft preparation, F.G. and T.V.; writing—review and editing, T.V. and O.W.; visualization, F.G. and T.V.; supervision, O.W.; This article is based on a chapter of F.G. dissertation in monograph form. All authors have read and agreed to the published version of the manuscript.

**Funding:** This research received no external funding.

**Data Availability Statement:** The raw data supporting the conclusions of this article will be made available by the authors on request.

**Conflicts of Interest:** The authors declare no conflict of interest.

## References

1. Gerland, F.; Wetzel, A.; Schomberg, T.; Wünsch, O.; Middendorf, B. A simulation-based approach to evaluate objective material parameters from concrete rheometer measurements. *Appl. Rheol.* **2019**, *29*, 130–140. [[CrossRef](#)]
2. Gerland, F.; Schomberg, T.; Kuhl, D.; Wünsch, O. Flow and Fiber Orientation of Fresh Fiber Reinforced Concrete. *PAMM* **2021**, *21*, e202100109. [[CrossRef](#)]
3. Gerland, F.; Schleiting, M.; Schomberg, T.; Wünsch, O.; Wetzel, A.; Middendorf, B. The Effect of Fiber Geometry and Concentration on the Flow Properties of UHPC. In *Rheology and Processing of Construction Materials*; Mechtcherine, V., Khayat, K., Secieru, E., Eds.; Series Title: RILEM Bookseries; Springer International Publishing: Cham, Switzerland, 2020; Volume 23, pp. 482–490. [[CrossRef](#)]
4. Ouari, N.; Kaci, A.; Tahakourt, A.; Chaouche, M. Rheological Behaviour of Fibre Suspensions in Non-Newtonian Fluids. *Appl. Rheol.* **2011**, *21*, 54801. [[CrossRef](#)]
5. Wang, Z.; Li, H.; Zhang, X.; Chang, Y.; Wang, Y.; Wu, L.; Fan, H. The Effects of Steel Fiber Types and Volume Fraction on the Physical and Mechanical Properties of Concrete. *Coatings* **2023**, *13*, 978. [[CrossRef](#)]
6. Villar, V.P.; Medina, N.F.; Alonso, M.; Diez, S.G.; Puertas, F. Assessment of parameters governing the steel fiber alignment in fresh cement-based composites. *Constr. Build. Mater.* **2019**, *207*, 548–562. [[CrossRef](#)]
7. Martinie, L.; Rossi, P.; Roussel, N. Rheology of Fiber Reinforced Cementitious Materials: Classification and Prediction. *Cem. Concr. Res.* **2010**, *40*, 226–234. [[CrossRef](#)]
8. Férec, J.; Bertevas, E.; Khoo, B.C.; Ausias, G.; Phan-Thien, N. The Effect of Shear-Thinning Behaviour on Rod Orientation in Filled Fluids. *J. Fluid Mech.* **2016**, *798*, 350–370. [[CrossRef](#)]
9. Folgar, F.; Tucker, C.L. Orientation Behavior of Fibers in Concentrated Suspensions. *J. Reinf. Plast. Compos.* **1984**, *3*, 98–119. [[CrossRef](#)]
10. Férec, J.; Mezi, D.; Advani, S.G.; Ausias, G. Axisymmetric Flow Simulations of Fiber Suspensions as Described by 3D Probability Distribution Function. *J. Non-Newton. Fluid Mech.* **2020**, *284*, 104367. [[CrossRef](#)]
11. Reinold, J.; Gudžulić, V.; Meschke, G. Computational modeling of fiber orientation during 3D-concrete-printing. *Comput. Mech.* **2023**, *71*, 1205–1225. [[CrossRef](#)]
12. Thanh, H.T.; Li, J.; Zhang, Y. Numerical modelling of the flow of self-consolidating engineered cementitious composites using smoothed particle hydrodynamics. *Constr. Build. Mater.* **2019**, *211*, 109–119. [[CrossRef](#)]
13. Zhao, Y.; Bi, J.; Wang, Z.; Huo, L.; Guan, J.; Zhao, Y.; Sun, Y. Numerical simulation of the casting process of steel fiber reinforced self-compacting concrete: Influence of material and casting parameters on fiber orientation and distribution. *Constr. Build. Mater.* **2021**, *312*, 125337. [[CrossRef](#)]
14. Rienesl, K.; Stelzer, P.S.; Major, Z.; Hsu, C.C.; Chang, L.Y.; Zulueta, K. Determination of fiber orientation model parameters for injection molding simulations via automated metamodel optimization. *Front. Mater.* **2023**, *10*, 1152471. [[CrossRef](#)]
15. Roussel, N. (Ed.) *Understanding the Rheology of Concrete*; Woodhead Publishing in Materials; Woodhead Publishing: Cambridge, UK, 2012.
16. Férec, J.; Bertevas, E.; Khoo, B.C.; Ausias, G.; Phan-Thien, N. A Rheological Constitutive Model for Semiconcentrated Rod Suspensions in Bingham Fluids. *Phys. Fluids* **2017**, *29*, 073103. [[CrossRef](#)]
17. Advani, S.G.; Tucker, C.L. The Use of Tensors to Describe and Predict Fiber Orientation in Short Fiber Composites. *J. Rheol.* **1987**, *31*, 751–784. [[CrossRef](#)]
18. Batchelor, G.K. The Stress Generated in a Non-Dilute Suspension of Elongated Particles by Pure Straining Motion. *J. Fluid Mech.* **1971**, *46*, 813–829. [[CrossRef](#)]

19. Dinh, S.M.; Armstrong, R.C. A Rheological Equation of State for Semiconcentrated Fiber Suspensions. *J. Rheol.* **1984**, *28*, 207–227. [[CrossRef](#)]
20. Chung, S.T.; Kwon, T.H. Coupled Analysis of Injection Molding Filling and Fiber Orientation, Including in-Plane Velocity Gradient Effect. *Polym. Compos.* **1996**, *17*, 859–872. [[CrossRef](#)]
21. Kugler, S.K.; Kech, A.; Cruz, C.; Osswald, T. Fiber Orientation Predictions—A Review of Existing Models. *J. Compos. Sci.* **2020**, *4*, 69. [[CrossRef](#)]
22. Schleiting, M.; Wetzels, A.; Gerland, F.; Niendorf, T.; Wunsch, O.; Middendorf, B. *Improvement of UHPFRC-Rheology by Using Circular Shape Memory Alloy Fibres*; Springer: Berlin/Heidelberg, Germany, 2019.
23. Schmidt, M.; Fehling, E.; Fröhlich, S. (Eds.) *Nachhaltiges Bauen mit ultra-hochfestem Beton: Ergebnisse des Schwerpunktprogrammes 1182 = Sustainable Building with Ultra-High Performance Concrete: Results of the German Priority Programme 1182*; Number 22 in Schriftenreihe Baustoffe und Massivbau; Kassel University Press: Kassel, Germany, 2014.
24. Favaloro, A.J.; Tucker, C.L. Analysis of Anisotropic Rotary Diffusion Models for Fiber Orientation. *Compos. Part A Appl. Sci. Manuf.* **2019**, *126*, 105605. [[CrossRef](#)]
25. Yun, M.; Argerich Martin, C.; Giormini, P.; Chinesta, F.; Advani, S. Learning the Macroscopic Flow Model of Short Fiber Suspensions from Fine-Scale Simulated Data. *Entropy* **2019**, *22*, 30. [[CrossRef](#)]
26. Chung, D.H.; Kwon, T.H. Invariant-Based Optimal Fitting Closure Approximation for the Numerical Prediction of Flow-Induced Fiber Orientation. *J. Rheol.* **2002**, *46*, 169–194. [[CrossRef](#)]

**Disclaimer/Publisher’s Note:** The statements, opinions and data contained in all publications are solely those of the individual author(s) and contributor(s) and not of MDPI and/or the editor(s). MDPI and/or the editor(s) disclaim responsibility for any injury to people or property resulting from any ideas, methods, instructions or products referred to in the content.